Wafer-Scale Performance Mapping of Magnetron-Sputtered Ternary Vanadium Tungsten Nitride for Microsupercapacitors

Khac Huy Dinh, Kevin Robert, Joelle Thuriot-Roukos, Marielle Huvé, Pardis Simon, David Troadec, Christophe Lethien, Pascal Roussel

Wafer-Scale Performance Mapping of Magnetron-Sputtered Ternary Vanadium Tungsten Nitride for Micro-supercapacitors

Khac Huy Dinh[1,2,3], Kevin Robert[1,3], Joelle Thuriot-Roukos[2], Marielle Huvé[2], Pardis Simon[2], David Troadec[1], Christophe Lethien[1,3,4*] and Pascal Roussel[2*]

[1] Institut d'Electronique, de Microélectronique et de Nanotechnologies, Université de Lille, CNRS, Université Polytechnique Hauts-de-France, UMR 8520 - IEMN, F-59000 Lille, France

[2] Unité de Catalyse et de Chimie du Solide (UCCS), Université de Lille, CNRS, Centrale Lille, Université d'Artois, UMR 8181 – UCCS, F-59000 Lille, France

[3] Réseau sur le Stockage Electrochimique de l'Energie (RS2E), CNRS FR 3459, 33 rue Saint Leu, 80039 Amiens Cedex, France

[4] Institut Universitaire de France (IUF), 75231 Paris Cedex, France

Abstract

To power Internet of Things applications, new materials are currently being investigated as efficient electrodes for micro-supercapacitor. In the recent years, multicationic materials were demonstrated to be an attractive new class of materials for electrodes. In this study, we deposited vanadium tungsten nitride by co-sputtering. Our film shows excellent electrochemical performance, a capacitance of 700 $F.cm^{-3}$ and no loss in capacitance retention after 5 000 cycles. In addition, the properties of the film were investigated in many aspects using advanced characterization techniques and mapping techniques. Our approach opens new perspectives and provides a powerful characterization tool for electrochemical materials.

Corresponding authors: christophe.lethien@univ-lille.fr and pascal.roussel@univ-lille.fr

Introduction

Today, we live in a world of internet-connected devices (the so-called Internet of Things) with various functions, i.e., healthcare, transportation, and agricultural monitoring[1]. However, to achieve smarter and more autonomous miniaturized devices, miniaturized energy storage devices are needed to power today's multi-functional integrated components[2]. In this context, besides Micro-Batteries (MB)[3], Micro-SuperCapacitors (MSCs) have been proposed as an efficient energy storage source for micro-devices used in Internet of Things applications[4]. Despite their high power densities, high rate capabilities and long-life cycling, MSCs still suffer from low energy density compared to MB[5]. To improve the energy density, increasing the working cell voltage, by either an asymmetric configuration or a hybrid MSC, is an interesting and promising solution[6–8]. In addition, enhancing the capacitance of electrode materials through research on capacitive materials (such as active carbon)[9], pseudocapacitive materials (conductive polymer, transition metal oxide or nitride)[10–13] or a new class of materials such as MXene series[14], multicationic[15] or multianionic[16] materials, is also a very fascinating approach.

Multicationic materials have recently gained more and more interest for MSCs electrode, due to their unique properties where different electroactive cations coexist in the same single crystal structure[17]. For instance, Achour et al. reported an optimized titanium-vanadium nitride thin film with Ti/V ratio close to 1.1 that achieved a capacitance of 15 $mF.cm^{-2}$ (410 $F.cm^{-3}$) without loss after 10 000 cycles[18]. Buvat et al. succeed in depositing $FeWO_4$ by sputtering method[19]. Their film showed 3.5 $mF.cm^{-2}$ (39 $F.cm^{-3}$) and a good capacitance retention after 10 000 cycles. Fe_2WO_6 was synthesized by Espinosa-Angeles et al. and showed a capacitance of 240 $F.cm^{-3}$ with an initial value of 85% after 10 000 cycles[17]. Jolayemi et al. reported $(Fe,Mn)_3O_4$ synthesized at RT (room temperature) by sputtering followed by post-annealing at 600 °C. Their film exhibited 15.5 $mF.cm^{-2}$ (155 $F.cm^{-3}$) of capacitance and stability after 10 000 cycles [20].

Beside the trial and error method, the predictive approach using DFT (Density-functional theory) theoretical calculations, is nowadays a very interesting approach to discover new materials. In that context, since our group had some experience in the synthesis of metal nitrides compounds[11,12], we decided to follow the extensive work of Sun et al.[21] who have systematically mapped predicted inorganic ternary nitrides (i.e. multicationic compounds). Among their predictions, they succeeded to experimentally validate, using magnetron sputtering deposition method, 7 new ternary nitrides (Zn-Mo-N, Zn-W-N, Zn-Sb-N, Mg-Ti-N,

Mg-Zr-N, Mg-Hf-N, Mg-Nb-N) and predicted more than 80 stable compounds, highlighting the interesting role of computational materials discovery in accelerating exploratory synthesis in novel chemical species.

Since both binary tungsten nitride and vanadium nitride are well-known efficient pseudocapacitive materials for MSCs[11,12,22,23], bimetallic V-W nitride phases (i.e. a ternary nitride film) are expected to present excellent electrochemical performance. We attempted to synthesize VWN_3, which is the only bimetallic V+W nitride phase expected to exist as a metastable phase, as predicted by Sun et al.[21] and reported in the Materials Project[24]. VWN_3 has been predicted as a 3D bimetallic V-W nitride crystallizing in P-1 space group a = 5.39 Å, b = 6.69 Å, c = 8.76 Å, α = 106.84 °, β = 87.76 °, ɣ = 102.54 ° (*Data retrieved from the Materials Project for VWN_3 (mp-1247461) from database version v2022.10.28.*). It is expected either improved capacitances or larger working potential window, and thus better performance if the two V and W cations are electroactive in the VWN_3 phase.

Ceder et al.[21] found nitrides to be the most metastable class of chemical compounds, because they have both the largest fraction of metastable phases and the highest average energies above the ground state phases. This unusual metastability has been attributed to the cohesivity afforded by strong metal-nitrogen bonds in the solid-state, which can kinetically 'lock-in' metastable nitride structures. Furthermore, thin-film fabrication is known as a synthesis technique remarkably capable of working out of the equilibrium state and thus stabilizing such a metastable nitride[25]. Consequently, in this study, the magnetron sputtering technique from V and W targets under Ar/N_2 atmosphere was used to study the formation of ternary nitride films with an ultimate goal to reach the expected VWN_3 phase.

To avoid duplicating the synthesis trials by varying the numerous parameters that govern the achievement of a film with both an optimal composition and microstructure, we decided to use a combinatorial magnetron sputtering approach. This relatively new approach has already been used in the discovery of novel superconducting materials based on Bi-Cu-Ca-Sr-Pb-Y-Ba oxide from sputtering targets by Xiang et al. [26] and blue photoluminescent material ($Gd_3Ga_5O_{12}$ on SiO_2 film) by Wang et al. [27]. Additionally, J.R. Dahn et al. [28], using magnetron sputtering combined with in situ masking, found a ternary film based on Si-Sn-Al elements as a negative electrode for Li-ion batteries, delivering up to 1800 $mAh.g^{-1}$. Thus, *in situ* rotational masking during the deposition process appears to be very useful method to obtain wide variety of materials on substrates, but has the major drawback of being complex to implement and requires physical masks that are difficult to manufacture.

Another approach applied in this paper was to perform high throughput syntheses using the rotation (or without rotation) of the substrate-holder during co-sputtering of two metal targets, namely a V target and a W target. Most of the time, it is crucial to have homogeneous deposition processes when a confocal setup is used. In contrast, if we do not rotate the sample-holder, a gradient of composition will be observed and thus, depending on the position on the wafer, various V_xW_y composition can be reached in the deposition made under argon atmosphere. Depending on the amount of nitrogen in the plasma, we thus can expect to reach the formation of numerous $V_xW_yN_z$ phases on road to stabilize the VWN_3 phase.

To evaluate the chemical, structural, mechanical, electrical, electrochemical, etc., properties on sputtered thin film at the wafer scale, we have also developed a high throughput characterization methodology, allowing mapping of thin $V_xW_yN_z$ films using micro-diffraction (XRD), micro-fluorescence (XRF), micro-Raman mapping, Eddy currents probing, and a home-made electrochemical mapping setup (for Cyclic Voltammetry (CV) and Electrochemical Impedance Spectroscopy (EIS) on 10 cm-diameter Si wafer coated with the $V_xW_yN_z$ films). This approach is emerging as an advanced and powerful characterization technique for studying electrode material (thin film) of miniaturized energy storage devices and more specifically for MSCs that could be collectively fabricated at the wafer scale.

Herein, we propose a study combining combinatorial magnetron sputtering of $V_xW_yN_z$ ternary films and high-throughput characterization methods to find the suitable electrode candidate for MSC. This co-sputtering approach allows a chemical composition gradient at the wafer scale using a sputtering platform in confocal configuration with a specific focus on the stabilization and isolation of the VWN_3 phase predicted by Ceder *et al* [21]. In parallel, we propose the development of a methodology to ensure the homogeneity (or not) of the deposits thus produced using a systematic approach of mapping of different complementary analytical techniques.

Material and methods

Sputtering deposition of $V_xW_yN_z$ thin films

Before any deposition, to prevent the etching of Si substrate by the 1M KOH electrolyte used in electrochemical experiments, a highly dense layer of Si_3N_4 (300 nm) was deposited by low-pressure chemical vapor deposition technique (LP CVD) at 800 °C (flow

rates: 60 sccm for NH_3 and 20 sccm for SiH_2Cl_2) on the top of Si wafer. Then $V_xW_yN_z$ was deposited on the substrate by reactive magnetron sputtering (Ar/N_2) from 2 pure 2 inches targets of vanadium and tungsten metal (99.9%) using a CT200 Alliance Concept reactor in confocal mode. Before the deposition, the pressure was kept below 10^{-6} mbar and the target-substrate distance was fixed at 6 cm. During deposition, the pressure, temperature and deposition time were fixed at 1.0×10^{-2} mbar, room temperature and 30 minutes, respectively. In this study, target power density and Ar / N_2 ratios were varied to optimize the microstructural and electrochemical properties. Nitrogen content was deducted from the flow rate ratio of N_2 / (Ar+N_2) (sccm). Two different approaches were used for the co-sputtering synthesis, depending on the expected goal: on the one hand, the substrate-holder was kept fixed in order to create a chemical composition gradient. On the other hand, at the optimal film composition, the substrate holder was rotated at 30 rpm to ensure good homogeneity of the structural, electrical and electrochemical properties.

Structural, chemical, electrical and morphological characterizations of the $V_xW_yN_z$ Thin Films

The morphology of $V_xW_yN_z$ thin films was determined using a Zeiss Ultra 55 scanning electron microscope (cross-section and top view analyses).

A Mettler Toledo XP6U microbalance was used to weight the amount of electroactive $V_xW_yN_z$ film and afterward determine the density of the films.

Electrical conductivity measurements were performed at the wafer scale by Eddy currents using Semilab WT 2000PVN contactless equipment.

TEM measurements were conducted on a S/TEM FEI TITAN Themis 300 equipped with a probe corrector for a resolution of 0.6 Å in STEM mode, and a Super-X quad EDS detector for elemental analysis. Prior to this, the sample had been thinned and mounted on a TEM copper grid using a FIB / SEM technique, so as to meet the requirements for TEM observation.

X-rays diffraction was performed using a 9kW rotating anode Rigaku Smartlab diffractometer in Bragg-Brentano geometry, delivering Cu Kα radiation (λ= 1.5418 Å) equipped with a Hypix 300 2D detector. A 2° offset of the substrate was applied to avoid detector saturation due to the high intensity of the (100) silicon peak. For mapping, an XYZ table was used in combination with a 400 µm CBO-f polycapillary.

A LabRAM HR800 Raman spectrometer (HORIBA Scientific, Jobin-Yvon) was employed to collect Raman spectra.

The X-ray Photoelectron Spectroscopy (XPS) experiments were carried out using a Kratos Axis Ultra DLD spectrometer, equipped with a monochromatic Al Kα X-ray source (1486.6 eV) operating at 225 W (15 kV, 15 mA). The instrument base pressure was 5.10^{-10} torr and the charge neutralizer system was used for all acquisitions. Analysis was performed at Pass Energy 20 eV and a step size of 0.05 eV. Binding Energies (BE) were referenced to C-C contribution in the C *1s* spectrum positioned at 284.8 eV. Simulation of the experimental photopeaks was carried out with CasaXPS software using mixed Gaussian (70%) / Lorentzian (30%) peaks except for metallic V-N and W-N contributions, where LA (1.2,5,8) and LA (1,4,15) line shape were respectively used. The line shape LA (a,b,n) offers asymmetric line-shapes based on the Lorentzian functional form convoluted with a Gaussian. Semiquantitative analysis was performed after the subtraction of Shirley type backgrounds.

Micro-X-ray fluorescence spectroscopy (XRF) mappings were carried out using a M4 Tornado 300 (Bruker) spectrometer equipped with an X-Ray tube Rhodium that uses a polycapillary lens offering a 200 µm spot size. The detector used was a Silicon-Drift-Detector cooled by a Peltier system (253°K). The measurement conditions were 50 kV and 600 µA for the Rh tube, chamber pressure 20 mbar and acquisition time 40 ms / pixel with a step size of 200 µm. The elements, that can be measured by this instrument unit range from sodium (Na) to uranium (U).

Electrochemical analyses

The electrochemical properties of $V_xW_yN_z$ electrodes were measured in a home-made Teflon cell, in a three-electrode configuration in 1M KOH aqueous electrolyte (Figure S1a, supplementary materials). The VN, WN or $V_xW_yN_z$ thin film, a platinum wire and the Hg/HgO reference acting as the working electrode (WE), the counter electrode and the reference electrode, respectively. Cyclic voltammetry (CV) and electrochemical impedance spectroscopy (EIS) were carried out on a Biologic VMP3 potentiostat / galvanostat equipment. For the EIS experiments, the measurements were performed at open circuit voltage between 100 kHz and 100 µHz frequency range considering a 50 mV rms sinusoidal voltage amplitude.

For mapping purposes, a home-made wafer scale measurement bench has been developed to allow 1 cm^2 spot CV and EIS measurements directly on the wafer without breaking it.

Results and discussion

$V_xW_yN_z$ films made with rotation of the substrate holder (classical approach)

Co-sputtering, an industrial thin film deposition method, has been shown to be efficient for producing ternary nitride films[18]. Therefore, as previously justified, co-sputtering technique was used to search for the metastable phase VWN_3 as predicted by Ceder et al.[21]. Figure 1a shows a schematic of the deposition setup. By controlling the power applied to the targets using a DC (Direct Current) generator to bias the V target and a RF (radio frequency) generator for the W target, the V/W composition ratio can be tuned to obtain the expected composition. Among other parameters such as pressure, target-substrate distance, temperature, gas flow, etc., the rotary stage is as an important factor in determining the homogeneity of the film composition. In the first part of this paper, it was rotated at a typical speed of 30 rpm (revolutions per minute) for expected homogeneous films. Since vanadium and tungsten nitrides[11,12,22,23,29] are already known as high performance electrode materials for MSCs, a combination of both performance are expected to have great potential for application in MSCs as electrodes[15,18–20]. We can also expect a better performance from this new VWN_3 material, i.e., an increase in the working potential window or surface capacitance compared to its constituent binary metal nitride (Figure 1b). The challenge is therefore to synthesize and stabilize the metastable sputtered VWN_3 film (see Figure 1c, which shows the predicted structural arrangement of VWN_3, alongside the VN and WN structural projections).

The influence of the sputtering power on the target was firstly studied, since it is directly related to the chemical composition of the resulting film (with a target V/W ratio equal to 1 in the VWN_3 phase). In a first step, the nitrogen content N_2 / (N_2+Ar) was fixed at 50 % in the plasma (flow of 15 sccm of N_2 and 15 sccm of Ar) at a pressure of 10^{-2} mbar with a 30° angle of the metallic targets, and a deposition time of 30 minutes. The W target power was chosen to be 2.96 $W.cm^{-2}$ (i.e., 60 W on a 2 inch target). The V target power was varied to obtain a V/W ratio equal to 1/1. Figure 2a shows the influence of the V target power on the V/W ratio, as determined by X-ray fluorescence technique (Figure S2 and S2.4). As the power

of the V target increases, the V/W ratio follows the same trend. It appears that at the same target power of 2.96 W.cm^{-2} for the tungsten one, the V/W is close to 1. Therefore, both target powers were fixed at 2.96 W.cm^{-2} and the nitrogen content were varied, while keeping the other parameters constant. The lattice parameter evolution versus N_2 content is shown in Figure 2b (typical diffractograms are given in Figure S3). At high N_2 content (> 50 %), the lattice parameter decreases from 4.23 Å to 4.18 Å, probably due to a larger amount of N_2 atoms inserted into the film, as already observed in literature [30]. At this stage, we can conclude that even if the V/W ratio is equal to one, the deposited film does not crystallize as expected, i.e., in a VWN_3 triclinic compound, but in a cubic Fm-3m one. This finding is not surprising since the VWN_3 phase is predicted to be metastable, as previously mentioned in the introduction. In order to overcome this problem, we annealed various samples under different conditions, but all of them failed to stabilize the expected structure (all the attempts with many different annealing conditions such as maximal temperature, heating rate, atmosphere – N_2, vacuum, air, different H_2 concentrations diluted in N_2 plasma are detailed in next section 2.3.2 and in the Figure S7 – S2.10).

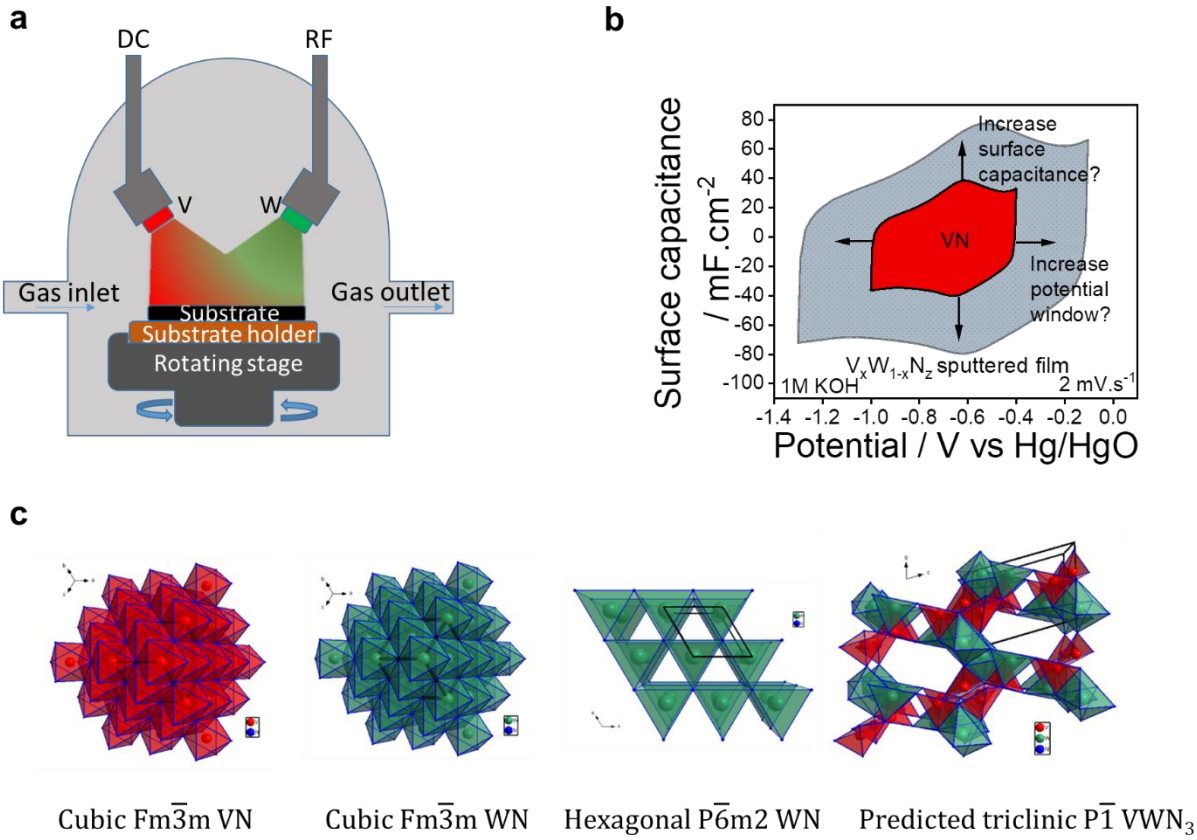

Figure 1 Overview of the $V_xW_yN_z$ synthesis process. (**a**) co-sputtering process. (**b**) Expected electrochemical performance of the VWN_3 metastable phase. (**c**) Polyhedral representations of

different V/W nitrides (V in red and W in green). From left to right: cubic Fm-3m VN, cubic Fm-3m WN, hexagonal P-6m2 WN, predicted triclinic P-1 VWN_3

The electrochemical behavior of the VWN_z film obtained with different N_2 contents (100 %, 83 %, 66 %, 50 % and 33 %) was then investigated by cyclic voltammetry (CV) in an aqueous electrolyte (1M KOH) at different scan rates (Figure S5 and S2.6). Figure 2c shows a typical CV at 2 $mV.s^{-1}$ of the sample with 33 % nitrogen content, which has a quasi-rectangular shape, indicating the pseudocapacitive behavior of the material[1]. The evolution of volumetric capacitance as a function of nitrogen content at different scan rates is shown in Figure 2d. The higher the nitrogen content in the film, the lower the capacitance, with the best value being 33 % following the same trends that we published previously on VN films resulting to a densification process [23]. At 2 $mV.s^{-1}$, the volumetric capacitance of the 33% nitrogen sample content is 700 $F.cm^{-3}$ (11.5 $mF.cm^{-2}$). The surface capacitance of such VWN_z thin film is higher than that of WN, but lower than that of VN using the same synthesis parameters (Figure 2e). However, this volumetric capacitance is one of the best reported so far for multicationic electrode materials for MSCs [18–20]. On the one hand, it is well-known that VN is an excellent electrode material for MSCs with a very high capacity, but on the other hand, depending on the synthesis conditions, the capacitance retention is not at its best level depending on the nitrogen content in the total gas. For VN films made by magnetron sputtering method, when the nitrogen content in the total gas is close to 17 %, 80 % of the initial capacitance is maintained during 50 000 cycles[22] while this capacitance retention is close to 100 % during 150 000 cycles when the nitrogen amount in the total gas is set to ~ 95 %[23]. It is an attractive solution for stabilizing the performance to set this nitrogen content in the total gas to 95 %, however, this results to a densification of the VN film, restricted the volumetric capacitance close to 400 $F.cm^{-3}$ instead of 700 $F.cm^{-3}$ for VN films deposited at a N_2 / (N_2 + Ar) ratio ~ 17%. A question arises now if it is not possible to stabilize the capacitance retention with “porous” films made at this N_2 / (Ar + N_2) ratio (17 %). In this study, Figure 2f shows that the co-sputtered VWN_z film electrode exhibits excellent stabilization as 100 % of capacitance retention is observed after 5000 cycles, whereas it was 70 % and 53 % for VN and W_2N, respectively. In VWN_z film, the tungsten seems to stabilize the performance in a similar way to what it was observed for $FeWO_4$ bulk electrode[15,31]. Additionally, we observed also that the capacitance value of VWN_z is better than the one of W_2N film showing the benefit from the ternary nitride configuration both from capacitance

and cycle lifetime point of view. Overall, this VWN_z film is a promising candidate for high-performance electrode material with excellent cycling ability and good capacitance.

In the present study, the VWN_z ternary nitride behaves as a good negative electrode in the working window between -1.0 V and -0.4 V vs Hg/HgO in 1M KOH electrolyte. Meanwhile, RuO_2 demonstrated the complimentary working window of -0.4 V to +0.15 V vs Hg/HgO in 1M KOH electrolyte[7]. Therefore, a VWN_z // RuO_2 asymmetric MSC could be considered for fabrication of such an asymmetric MSC to boost the performance of MSC.

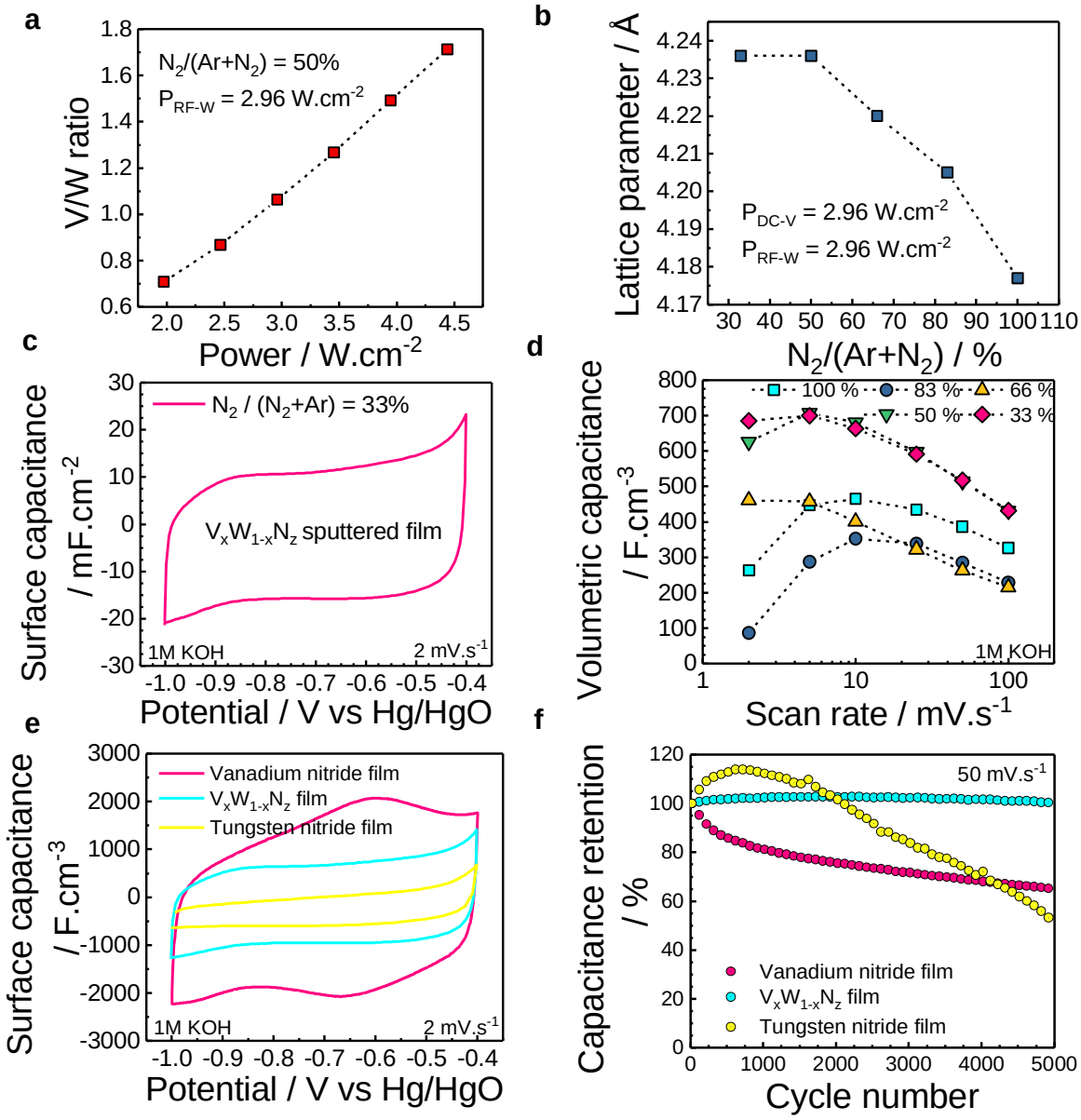

Figure 2 VWN_z thin film study with the substrate rotation during deposition. (**a**) V target power versus V/W ratio. (**b**) Effect of nitrogen content to lattice parameter. (**c**) Typical CV of VWN_z film at 2 $mV.s^{-1}$ in 1M KOH. (**d**) Volumetric capacitance of various nitrogen content

samples. (**e**) CV of vanadium nitride, tungsten nitride and VWN_z film. (**f**) Capacitance retention of vanadium nitride, tungsten nitride and VWN_z film.

Combinatory magnetron sputtering combined with advanced mapping techniques

Since classical co-sputtering process with rotation of the substrate holder did not produce the expected VWN_3 phase, a combinatory approach without the rotation of substrate holder (speed = 0 rpm) was used to search for the expected VWN_3 phase while keeping the target power similar to the previous study of V and W target at 2.96 $W.cm^{-2}$ (reminder: V/W has to be equal to 1 in VWN_3). By doing that, the composition gradient can be obtained directly with sputtered films deposited on 3'' silicon wafer

Figure 3a shows a top surface analysis of the coated Si wafer made by XRF mapping in order to evaluate the chemical composition on the film. In this XRF top view analysis, the resolution of the mapping technique allows to have a very accurate evaluation of the chemical composition because a full spectrum is measured every 20 µm that can be transformed into a V and/or W chemical stoichiometry mapping (in red and green respectively). The gradient of chemical composition is clearly visible due to the absence of rotation, with green corresponding to the W-rich zone and red to the V-rich zone. Six different zones of the wafer were considered (the six white oval shapes in Figure 3a) and the chemical composition in each zone was averaged (see results in Figure S4). In addition, the effect of N_2 content on the composition was investigated for each zone (Figure 3b). It appears that the V/W ratios are close to 1 (always the expected ratio for the expected VWN_3 triclinic phase) at various nitrogen content in the total gas ratio: in the zone 2 for the 66 % ratio and at zone 4 for both 50 % and 33 % ratios. These particular positions carefully studied by applying a post-deposition annealing to further crystallize the film in search of the metastable VWN_3 phase. First, high temperature was used for annealing under primary vacuum, but unfortunately vanadium and tungsten oxides were obtained after 2h at 1000°C, even after several purging/pumping cycles (Figure S8a). It might due to the oxygen content remaining in the annealing chamber and the surface of the film after exposing to ambient air. Then, a pure nitrogen atmosphere was tried, but in this case, after a 2h plateau at 800°C, the diffractogram remained unchanged. In the same atmosphere, after 2h at 1000°C, oxides were formed (Figure S8b). Therefore, an *in situ* high-temperature X-ray diffraction experiment was carry out, but the conclusion is the same as for ex situ annealing, i.e., that the cubic Fm-3m VWN_z phase

transforms into oxides at high temperature, without intermediate formation of the expected triclinic P-1 VWN_3 phase. To avoid this oxidation problem, it was proposed by Houmes et al.[32] that small amounts of hydrogen in plasma could remove oxygen impurities. Thus, a 95% N_2 + 5% H_2 atmosphere was used (Figure S8c). After a 2h plateau at 1000°C in this atmosphere, almost all of the initial phase was reduced to a metallic VW phase. To limit the reducing capacity of this atmosphere, we decreased both the amount of H_2 to 3% and the temperature to 700°C, but even though the amount of metallic phase was reduced, the conclusion remained the same. Finally, at 1% H_2 and 700°C, VN and WN seemed to demix, but the expected VWN_3 was unable to form. Unfortunately, the operating conditions allowing to stabilize this phase were not found after many tests so the experiments were stopped.

However, we have continued to characterize our samples at wafer scale by mapping, as we believe that this is an interesting approach that greatly reduces the number of samples to be synthesized when it comes to optimizing a chemical composition. Moreover, this method is not only sophisticated but also cost-effective and time-efficient.

Advanced mapping methods using a variety of complementary techniques allows to evaluate the various properties of $V_xW_yN_z$ films and able to correlate the different properties. For example, the electrical conductivity of the 33 % nitrogen wafer is shown in Figure 3c. This result is quite consistent as tungsten nitride has a higher conductivity than vanadium (11.1×10^6 and 1.17×10^6 $S.m^{-1}$, respectively) [33], and similar behavior is observed in chemical mapping where higher conductivity corresponds to higher W content in the micro-XRF map [22].

A typical micro-XRD diffractogram of the $V_xW_yN_z$ film corresponding to position 3 in the wafer is shown in Figure 3d. The peaks at 2θ = 36.6°, 42.7°, 62.3°, 73.9° and 78.2° correspond to planes (111), (200), (220), (311) and (222) respectively, assigned to the cubic Fm-3m structure, a = 4.22 Å. It shows only one set of peaks that could be due to either a solid solution or an epitaxial growth of VN on WN (or the opposite, WN on VN). As demonstrated by TEM, this epitaxial possibility was ruled out (see after). For the micro-diffraction mapping experiment, one pattern was recorded every 5 mm on the whole wafer (Figure S3). The integrated intensity of the (111) diffraction was extracted from the diffractograms and plotted vs the X-Y position of the beam on the 3" wafer (Figure 3e). This result clearly shows that the most intense peak is found near the higher W composition position (green area) in the chemical mapping. Assuming the hypothesis of the absence of a preferred orientation in our film, this can be interpreted as a quite expected behavior, since in such a solid solution with

both V and W, the position with the largest amount of W (higher Z) will have a higher structure factor and hence a higher diffracted intensity.

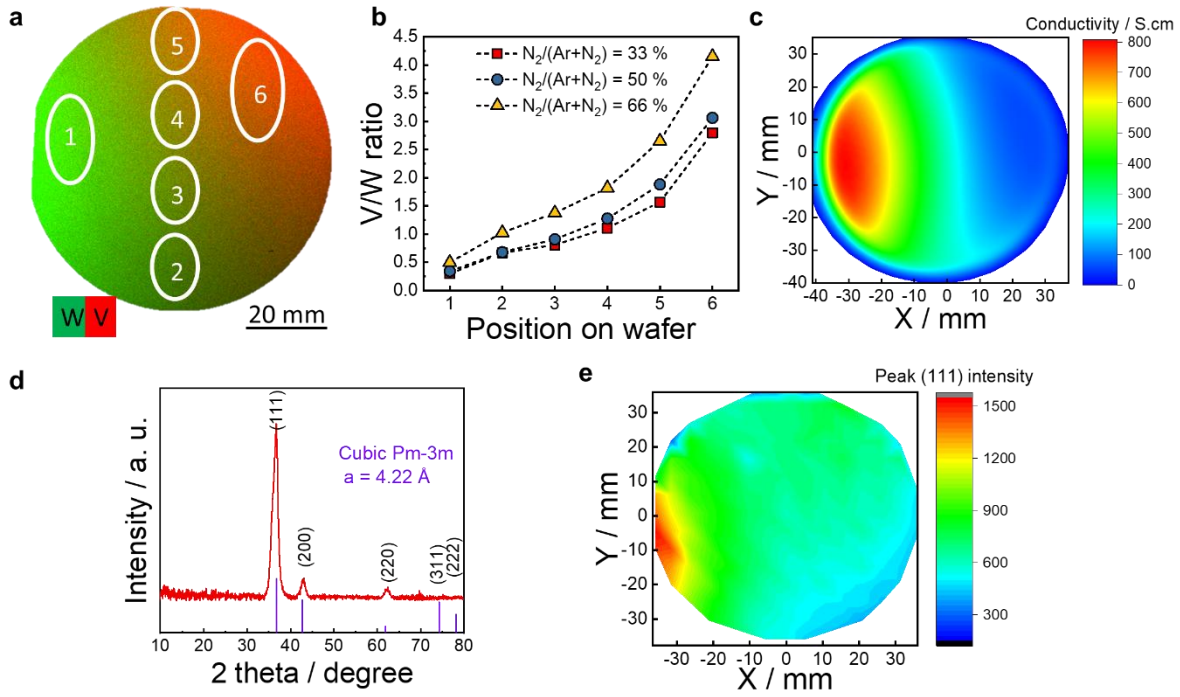

Figure 3 $V_xW_yN_z$ thin film without rotating during deposition. (**a**) XRF map. (**b**) Effect of nitrogen content to V/W ratio of different position of wafer. (**c**) Electrical conductivity map (**d**) Typical X-ray diffractogram. (**e**) Peak (111) intensity map extracted from XRD.

A Raman spectroscopy mapping analysis is shown in Figure 4a. The identical peaks of the V-N bonds are observed at 130, 263, and 983 cm^{-1} [34] while W-N bonds are observed at 804 cm^{-1} [35]. Although Raman is a non-quantitative method, the positions and intensities of the peaks vary with the position of the analyses on the wafer. For example, the W-N-W bond at 804 cm^{-1} dominates in zone 1, i.e., close to the high W content, whereas, in contrast, in zone 6, close to the high V content, the peak is weak. This might also indicate a variation in chemical composition with respect to the positions on the wafer.

The electrochemical CVs mapping is shown in Figure 4b. The area of the curves varies with the position on the wafer. There is also a tendency for wider CVs or higher capacitances to be related to a position with higher V content. The surface capacitance calculated at zone 5 (high V content) is 20.3 $mF.cm^{-2}$ while it is only 1 $mF.cm^{-2}$ at zone 1 (high W content). This is attributed to the better performance of vanadium nitride compared to tungsten, when it concerns the surface capacitance [12,23]. The EIS mapping by Nyquist plot is shown in Figure S12. It can be seen a variation of the equivalent serial resistance probably correlated to the electrical conductivity variation of the sputtered film (Figure S11).

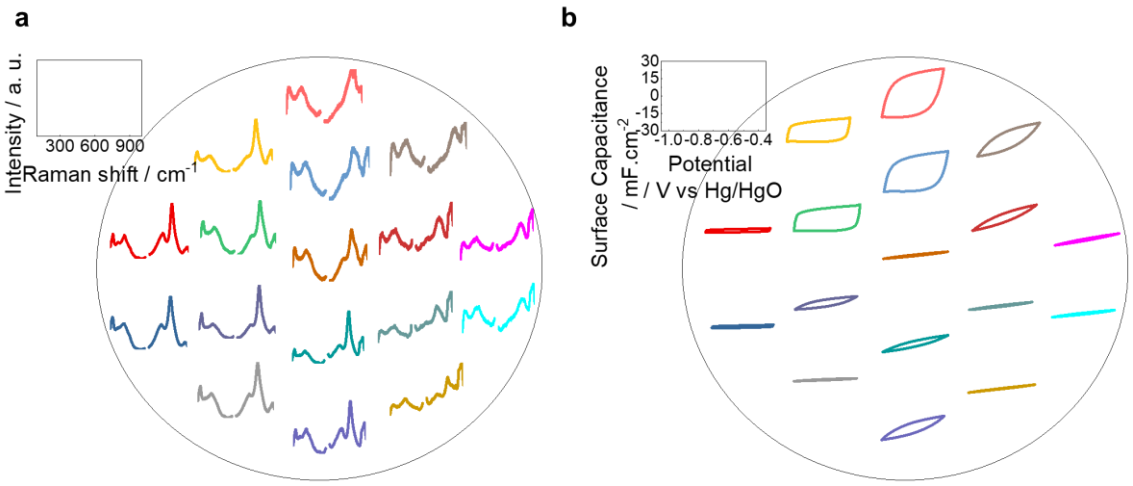

Figure 4 Mapping $V_xW_yN_z$ thin film without rotating during deposition (**a**) Raman spectroscopy map. (**b**) Electrochemical CV mapping at 25 $mV.s^{-1}$ in 1M KOH aqueous electrolyte.

At this stage, some partial conclusions can be drawn from this study. Firstly, even after many synthesis attempts (whatever the position on the wafer, i.e. with different chemical compositions, or whatever the post-annealing conditions for the 1/1 ratio between V and W), we have not been able to stabilize the P-1 VWN_3 phase predicted by Ceder et al[21]. It might due to the thermodynamic and/or kinetic conditions are too far from those tested in the frame of this study where the deposition pressure could maybe set to the lowest value (10^{-3} mbar) in order to limit the columnar morphology of the films. However, by using confocal co-sputtering deposition method without substrate rotation, we open the way to a new combinatorial approach for designing nice sputtered films acting as an electrode material and current collector for MSC that allows a strong reduction in successive depositions, thus avoiding the synthesis of a large number of samples (saving time and money). Finally, in order to study such a compositional gradient at the wafer scale, we had to develop tools that allow complementary characterization techniques, also at the wafer scale that can be used for many other applications, such as the collective fabrication of micro-devices on large scale wafer.

Co-sputtered homogenous VWN_z films on Si wafer

In the previous part, we showed that thin films deposited by co-sputtering approach (V and W targets bias both at 2.96 $W.cm^{-2}$, with 33 % nitrogen content and a substrate holder rotation of 30 rpm) gave the best electrochemical properties among other samples (700 $F.cm^{-}$

[3], 100 % capacitance retention). As it is important to check the homogeneity of the deposition, a full characterization of the VWN_z film based on this optimized set of parameters was carried out by our mapping techniques (XRF, XRD, electrical conductivity, Raman spectroscopy, CV and EIS) and by additional techniques such as XPS and electron microscopy (SEM/TEM).

The chemical micro-XRF map is shown in Figure 5a confirming the homogeneous deposition of V and W on the wafer (for comparison without rotation, see Figure S2). The homogeneous film deposition is also confirmed by both the conductivity map and the intensity distribution of the (111) diffraction peak vs X-Y position in Figure S11. The Raman spectroscopy map is shown in Figure 6a. The identical peak of V-N bonds can also be seen at 130, 263, and 983 cm^{-1} [34], while W-N bonds are observed at 804 cm^{-1} [35]. Compared to the gradient composition of sample deposited without rotation (see Figure 4a), the peak position and intensity are more similar at different positions. Figure 6b shows the electrochemical mapping of the VWN_z sample made by CV techniques. There is a difference in position * and **, maybe due to an error occurring during the measurement (not possible to make again the mapping because the sample was cut to check the film morphology by SEM cross section analyses). Overall, the CV shape is quasi-rectangular and similar in all positions on the wafer. The surface capacitance calculated at different spots in the wafer (except for position * and **) varied in small range 11 - 17 $mF.cm^{-2}$. The different in capacitance is only 1.5-fold compared to the 20-fold one observed for sample without rotation (range from 1 to 20 $mF.cm^{-2}$). The EIS map in Figure S12 shows similar behavior. All these mappings confirm the homogeneity at the wafer scale for the 30-rpm rotated substrate.

Finally, to fully characterize this optimized film, some complementary techniques such as TEM and XPS were performed, this time not at mapping scale but at a local scale. Cross-sections of a $Si/Si_3N_4/VWN_z$ stack were obtained made by FIB. Figure 5b and Figure S13, S2.14 shows the HAADF (High Angle Annular Dark Field) contrast image of the thin film, illustrating the formation of columnar morphology with interspacing between them, as already observed for VN and WN [11,12]. This peculiar porous morphology is indeed well adapted to such micro-devices whose performance is mainly related to redox reactions taking place at the surface of the materials [36]. Above the 100 nm-thick Si_3N_4 protective layer, the film thickness is ~ 150 nm, which corresponds to a growth rate of 5 nm/min. The HRTEM images (Figure S13) display a polycrystalline VWN_z layer, which is more compact at the bottom. EDS maps (Figure 5b ii - vii and S2.14) carried out at the nanometer scale confirm the stacking and the perfect interfaces between the different layers. It shows that V and W elements are randomly distributed throughout the entire film. Note that the small layer of SiO_2

growth naturally on Si due to exposed to ambient air (Figure 5b vi) and presence of Si in the VWN_z layer map is due to the energy overlap of the KαSi and MαW lines (Figure 5c).

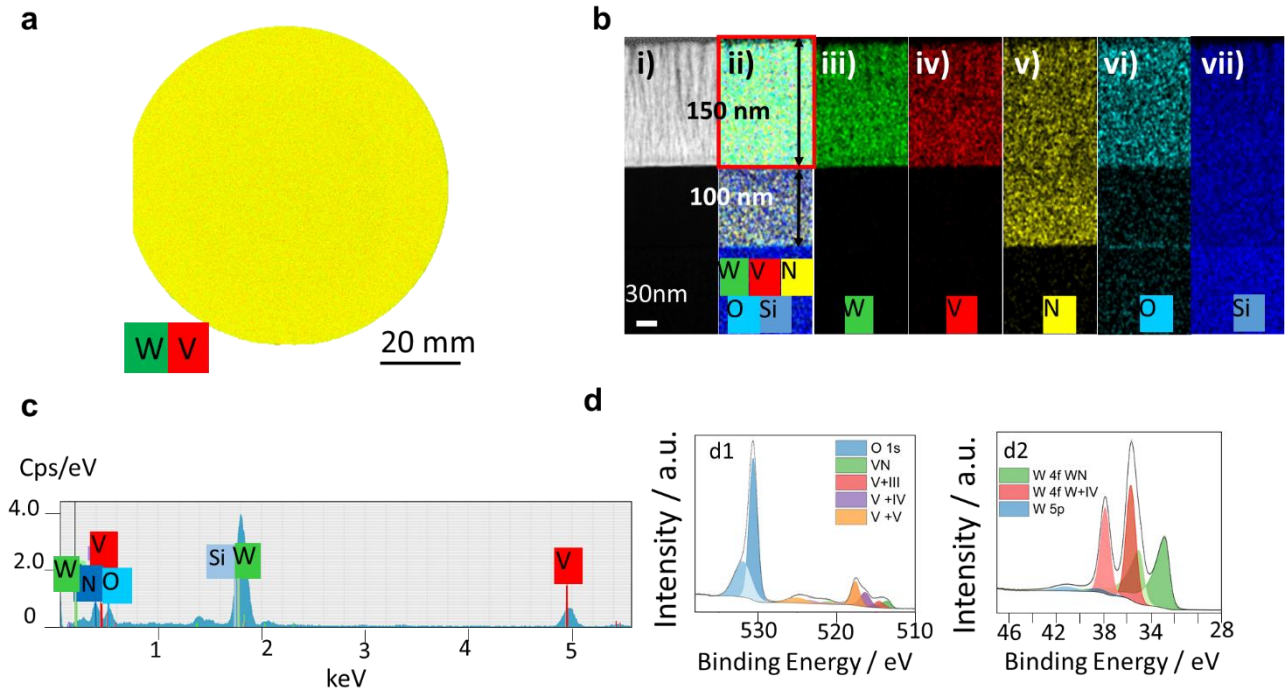

Figure 5 Characterization of the 33 % nitrogen sample (optimal composition) with rotation of the substrate during deposition. (**a**) Micro-XRF map. (**b**) HAADF - TEM analysis. (**c**) EDX analysis of red box part on (**b**). (**d**) High resolution XPS spectra of V and W core level.

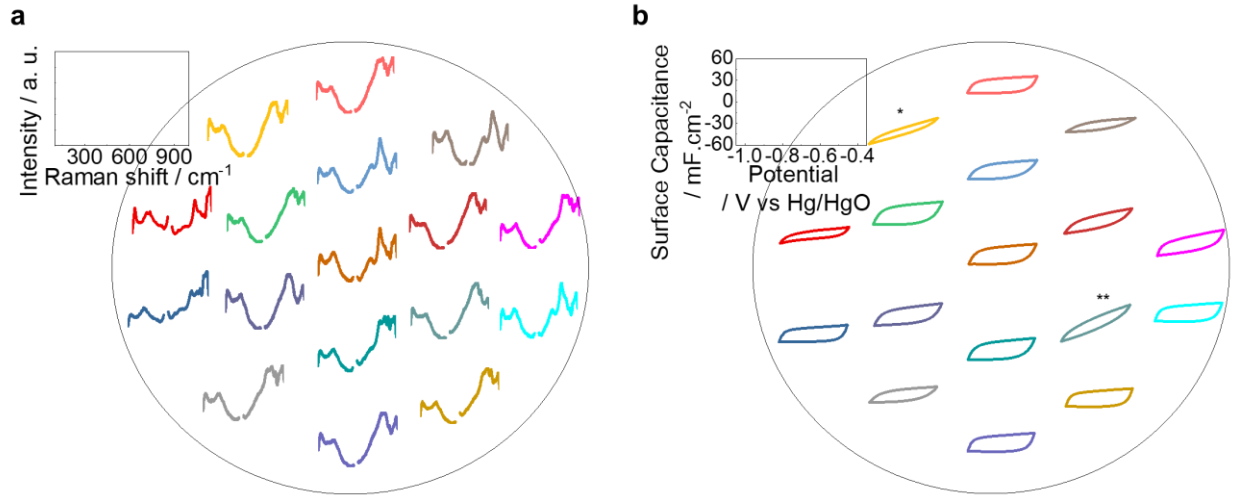

Figure 6 Mapping of the 33 % nitrogen sample with rotation of the substrate during deposition. (**a**) Raman mapping at different points on the wafer (**b**) Electrochemical mapping by CV (scan rate 25 $mV.s^{-1}$ in 1M KOH aqueous electrolyte).

The high resolution XPS spectra (V *2p* and W *4f* core-level region) of the VWN_z film are shown in Figure 5d. As already discussed in detail in literature [22], the V *2p* core level is rather complex due to a Coster-Kronig effect and has been decomposed following the same logic than in [22], showing the presence of vanadium nitride at low BE (binding energy) and three vanadium oxides and/or oxynitride with oxidation states +III, +IV and +V. Regarding the W *4f* orbital, it can be decomposed into 2 doublet peaks with energy splitting 2.18 eV and W $4f_{7/2}$ BEs equal to 32.8 eV and 35.7 eV. The low BE, asymmetrical contribution is attributed to the presence of WN species, whereas the high BE contribution is attributed to the formation of W oxide with +VI oxidation state, in agreement with ref [12]. Two additional low intensity peaks at 38.3 eV and 41.2 eV are attributed respectively to the WN and W^{+VI} W $5p_{5/2}$ contributions. Finally, a relative surface V/W atomic ratio of 0.47 is calculated, as expected from the targeted nominal ratio.

Conclusion

In this study, we deposited vanadium tungsten nitride by co-sputtering deposition method. By tuning the rotation during sputtering process, gradient and homogenous composition are used to search for predicted metastable phase VWN_3. We were unable to synthesis the phase, however, our VWN_z film shows excellent electrochemical performance among multicationic material for MSC. It reached a volumetric capacitance value of 700 $F.cm^{-3}$ and no loss of the initial capacitance after 5 000 cycles. We found also that the tungsten element was able to stabilize the cycling stability of vanadium nitride-based films at low nitrogen content to the total gas. We developed a set of advanced characterization technique by using different mapping techniques to evaluate the properties of the VWN_z film. Our approach can open new perspectives and provide a powerful characterization tool for the discovery and the full characterization of the novel electrode materials for MSC.

Supporting information

Supplementary data associated with this article can be found in the online version at …

Electrochemical analysis equipment; XRF measurement; XRD micro-diffraction; XRF analysis of VWN sample at different area on the deposited wafer; VWN with rotate during deposition as function of N_2 content; VWN sample compared to VN and W_2N thin films reference at same fabrication conditions; Post annealing by thermal diffraction; Post annealing of VWN at different environment; Post annealing of VWN with rotate during deposition; Post annealing of VWN with rotate during deposition in mixture of nitrogen and hydrogen at various temperatures; Mapping analysis; EIS mapping by Nyquist plot; HRTEM of the film HAADF images and EDS maps.

Acknowledgments

K.H.D acknowledges funding from the European Union's Horizon 2020 research and innovation program under the Marie Sklodowska-Curie grant agreement no. 847568. The authors thank the French National Research Agency (STORE-EX Labex Project ANR-10-LABX-76-01 and ARTEMIS ANR project ANR-22-ASEN-0001-01). The French RENATECH network and the University of Lille are greatly acknowledged for supporting the Center of MicroNanoFabrication (CMNF) facility from IEMN. Chevreul Institute (FR 2638) is acknowledged for supporting XRD and TEM facility. REALCAT platform is acknowledged for supporting XRF facility. Finally, Bukola Jolayemi (IEMN) is also thanked for fruitful discussions.

References

(1) Lethien, C.; Le Bideau, J.; Brousse, T. Challenges and Prospects of 3D Micro-Supercapacitors for Powering the Internet of Things. *Energy Environ. Sci.* **2019**, *12* (1), 96–115. https://doi.org/10.1039/c8ee02029a.

(2) Dinh, K. H.; Roussel, P.; Lethien, C. Advances on Microsupercapacitors: Real Fast Miniaturized Devices toward Technological Dreams for Powering Embedded Electronics? *ACS Omega* **2023**, *8* (10), 8977–8990. https://doi.org/10.1021/acsomega.2c07549.

(3) Létiche, M.; Eustache, E.; Freixas, J.; Demortière, A.; De Andrade, V.; Morgenroth, L.; Tilmant, P.; Vaurette, F.; Troadec, D.; Roussel, P.; Brousse, T.; Lethien, C. Atomic Layer Deposition of Functional Layers for on Chip 3D Li-Ion All Solid State Microbattery. *Adv. Energy Mater.* **2017**, *7* (2), 1–12. https://doi.org/10.1002/aenm.201601402.

(4) Raj, A.; Steingart, D. Review—Power Sources for the Internet of Things. *J. Electrochem. Soc.* **2018**, *165* (8), B3130–B3136. https://doi.org/10.1149/2.0181808jes.

(5) Simon, P.; Gogotsi, Y. Perspectives for Electrochemical Capacitors and Related Devices. *Nat. Mater.* **2020**, *19* (11), 1151–1163. https://doi.org/10.1038/s41563-020-0747-z.

(6) Naderi, L.; Shahrokhian, S.; Soavi, F. Fabrication of a 2.8 v High-Performance Aqueous Flexible Fiber-Shaped Asymmetric Micro-Supercapacitor Based on MnO2/PEDOT:PSS-Reduced Graphene Oxide Nanocomposite Grown on Carbon Fiber Electrode. *J. Mater. Chem. A* **2020**, *8* (37), 19588–19602. https://doi.org/10.1039/d0ta06561g.

(7) Asbani, B.; Robert, K.; Roussel, P.; Brousse, T.; Lethien, C. Asymmetric Micro-Supercapacitors Based on Electrodeposited Ruo2 and Sputtered VN Films. *Energy Storage Mater.* **2021**, *37* (February), 207–214. https://doi.org/10.1016/j.ensm.2021.02.006.

(8) Sallaz, V.; Poulet, S.; Rouchou, J.; Boissel, J. M.; Chevalier, I.; Voiron, F.; Lamy, Y.; Oukassi, S. Hybrid All-Solid-State Thin-Film Micro-Supercapacitor Based on a Pseudocapacitive Amorphous TiO2 Electrode. *ACS Appl. Energy Mater.* **2023**, *6* (1), 201–210. https://doi.org/10.1021/acsaem.2c02742.

(9) Huang, P.; Lethien, C.; Pinaud, S.; Brousse, K.; Laloo, R.; Turq, V.; Respaud, M.; Demortière, A.; Daffos, B.; Taberna, P. L.; Chaudret, B.; Gogotsi, Y.; Simon, P. On-Chip and Freestanding Elastic Carbon Films for Micro-Supercapacitors. *Science (80-.).* **2016**, *351* (6274), 691–695. https://doi.org/10.1126/science.aad3345.

(10) Chu, X.; Chen, G.; Xiao, X.; Wang, Z.; Yang, T.; Xu, Z.; Huang, H.; Wang, Y.; Yan, C.; Chen, N.; Zhang, H.; Yang, W.; Chen, J. Air-Stable Conductive Polymer Ink for Printed Wearable Micro-Supercapacitors. *Small* **2021**, *17* (25), 1–8. https://doi.org/10.1002/smll.202100956.

(11) Robert, K.; Douard, C.; Demortière, A.; Blanchard, F.; Roussel, P.; Brousse, T.; Lethien, C. On Chip Interdigitated Micro-Supercapacitors Based on Sputtered Bifunctional Vanadium Nitride Thin Films with Finely Tuned Inter- and Intracolumnar Porosities. *Adv. Mater. Technol.* **2018**, *3* (7), 1–12. https://doi.org/10.1002/admt.201800036.

(12) Ouendi, S.; Robert, K.; Stievenard, D.; Brousse, T.; Roussel, P.; Lethien, C. Sputtered Tungsten Nitride Films as Pseudocapacitive Electrode for on Chip Micro-Supercapacitors. *Energy Storage Mater.* **2019**, *20* (February), 243–252. https://doi.org/10.1016/j.ensm.2019.04.006.

(13) Ferris, A.; Bourrier, D.; Garbarino, S.; Guay, D.; Pech, D. 3D Interdigitated Microsupercapacitors with Record Areal Cell Capacitance. *Small* **2019**, *15* (27), 1–8. https://doi.org/10.1002/smll.201901224.

(14) Huang, H.; Chu, X.; Xie, Y.; Zhang, B.; Wang, Z.; Duan, Z.; Chen, N.; Xu, Z.; Zhang, H.; Yang, W. Ti3C2TxMXene-Based Micro-Supercapacitors with Ultrahigh Volumetric Energy Density for All-in-One Si-Electronics. *ACS Nano* **2022**, *16* (3), 3776–3784. https://doi.org/10.1021/acsnano.1c08172.

(15) Crosnier, O.; Goubard-Bretesché, N.; Buvat, G.; Athouël, L.; Douard, C.; Lannelongue, P.; Favier, F.; Brousse, T. Polycationic Oxides as Potential Electrode Materials for Aqueous-Based Electrochemical Capacitors. *Curr. Opin. Electrochem.* **2018**, *9*, 87–94. https://doi.org/10.1016/j.coelec.2018.05.005.

(16) Kageyama, H.; Hayashi, K.; Maeda, K.; Attfield, J. P.; Hiroi, Z.; Rondinelli, J. M.; Poeppelmeier, K. R. Expanding Frontiers in Materials Chemistry and Physics with Multiple Anions. *Nat. Commun.* **2018**, *9* (1). https://doi.org/10.1038/s41467-018-02838-4.

(17) Espinosa-Angeles, J. C.; Goubard-Bretesché, N.; Quarez, E.; Payen, C.; Sougrati, M. T.; Crosnier, O.; Brousse, T. Investigating the Cycling Stability of Fe2wo6

Pseudocapacitive Electrode Materials. *Nanomaterials* **2021**, *11* (6), 1–11. https://doi.org/10.3390/nano11061405.

(18) Achour, A.; Lucio-Porto, R.; Chaker, M.; Arman, A.; Ahmadpourian, A.; Soussou, M. A.; Boujtita, M.; Le Brizoual, L.; Djouadi, M. A.; Brousse, T. Titanium Vanadium Nitride Electrode for Micro-Supercapacitors. *Electrochem. commun.* **2017**, *77*, 40–43. https://doi.org/10.1016/j.elecom.2017.02.011.

(19) Buvat, G.; Iadecola, A.; Blanchard, F.; Brousse, T.; Roussel, P.; Lethien, C. A First Outlook of Sputtered FeWO 4 Thin Films for Micro-Supercapacitor Electrodes . *J. Electrochem. Soc.* **2021**, *168* (3), 030524. https://doi.org/10.1149/1945-7111/abec57.

(20) Jolayemi, B.; Buvat, G.; Brousse, T.; Roussel, P.; Lethien, C. Sputtered (Fe,Mn) 3 O 4 Spinel Oxide Thin Films for Micro-Supercapacitor . *J. Electrochem. Soc.* **2022**, *169* (11), 110524. https://doi.org/10.1149/1945-7111/aca050.

(21) Sun, W.; Bartel, C. J.; Arca, E.; Bauers, S. R.; Matthews, B.; Orvañanos, B.; Chen, B. R.; Toney, M. F.; Schelhas, L. T.; Tumas, W.; Tate, J.; Zakutayev, A.; Lany, S.; Holder, A. M.; Ceder, G. A Map of the Inorganic Ternary Metal Nitrides. *Nat. Mater.* **2019**, *18* (7), 732–739. https://doi.org/10.1038/s41563-019-0396-2.

(22) Robert, K.; Stiévenard, D.; Deresmes, D.; Douard, C.; Iadecola, A.; Troadec, D.; Simon, P.; Nuns, N.; Marinova, M.; Huvé, M.; Roussel, P.; Brousse, T.; Lethien, C. Novel Insights into the Charge Storage Mechanism in Pseudocapacitive Vanadium Nitride Thick Films for High-Performance on-Chip Micro-Supercapacitors. *Energy Environ. Sci.* **2020**, *13* (3), 949–957. https://doi.org/10.1039/c9ee03787j.

(23) Jrondi, A.; Buvat, G.; Pena, F. D. La; Marinova, M.; Huvé, M.; Brousse, T.; Roussel, P.; Lethien, C. Major Improvement in the Cycling Ability of Pseudocapacitive Vanadium Nitride Films for Micro-Supercapacitor. *Adv. Energy Mater.* **2023**, *2203462*, 1–16. https://doi.org/10.1002/aenm.202203462.

(24) Jain, A.; Ong, S. P.; Hautier, G.; Chen, W.; Richards, W. D.; Dacek, S.; Cholia, S.; Gunter, D.; Skinner, D.; Ceder, G.; Persson, K. A. Commentary: The Materials Project: A Materials Genome Approach to Accelerating Materials Innovation. *APL Mater.* **2013**, *1* (1). https://doi.org/10.1063/1.4812323.

(25) Červená, M.; Čerstvý, R.; Dvořák, T.; Rezek, J.; Zeman, P. Metastable Structures in Magnetron Sputtered W–Zr Thin-Film Alloys. *J. Alloys Compd.* **2021**, *888*, 161558. https://doi.org/10.1016/j.jallcom.2021.161558.

(26) Xiang, X.; Choquette, K. D.; Efstathiadis, H.; LaComb, L.; Ray, H. S. Bi-Cu-Ca-Sr-Pb-Y-Ba Oxide Superconducting Thin Films by Sequential Sputtering. *Science (80-.).*

1995, *268* (5210), 1738–1740. https://doi.org/10.1126/science.268.5210.1738.

(27) Wang, D.; Han, J.; Takebe, M.; Nakagawa, T.; Miyamoto, Y. Combinatorial Search for a Blue-Emitting Phosphor: Stabilization of Gd3Ga5O12 by SiO2 Coating. *Science (80-.).* **1998**, *279* (5355), 335–337. https://doi.org/10.1126/science.279.5355.335.

(28) Dahn, J. R.; Marom, R.; Israelachvili, J. High-Rate Lithium-Insertion Ternary Alloys Made from Mixed Oxides. *Electrochem. solid-state Lett.* **2003**, *6* (5), A75–A79. https://doi.org/10.1149/1.1563094.

(29) Choi, C.; Robert, K.; Whang, G.; Roussel, P.; Lethien, C.; Dunn, B. Photopatternable Hydroxide Ion Electrolyte for Solid-State Micro-Supercapacitors. *Joule* **2021**, *5* (9), 2466–2478. https://doi.org/10.1016/j.joule.2021.07.003.

(30) Cao, Z.; Jin, N.; Ye, J.; Du, X.; Liu, Y. First-Principles Study on the Effects of N and Al Doping on the Mechanical Properties and Electronic Structures of TiC. *RSC Adv.* **2020**, *10* (60), 36295–36302. https://doi.org/10.1039/d0ra06630c.

(31) Goubard-Bretesché, N.; Crosnier, O.; Douard, C.; Iadecola, A.; Retoux, R.; Payen, C.; Doublet, M. L.; Kisu, K.; Iwama, E.; Naoi, K.; Favier, F.; Brousse, T. Unveiling Pseudocapacitive Charge Storage Behavior in FeWO4 Electrode Material by Operando X-Ray Absorption Spectroscopy. *Small* **2020**, *16* (33), 2–9. https://doi.org/10.1002/smll.202002855.

(32) Houmes, J. D.; Zur Loye, H. C. Microwave Synthesis of Ternary Nitride Materials. *J. Solid State Chem.* **1997**, *130* (2), 266–271. https://doi.org/10.1006/jssc.1997.7303.

(33) Sun, Z.; Zhang, J.; Yin, L.; Hu, G.; Fang, R.; Cheng, H.-M.; Li, F. Conductive Porous Vanadium Nitride/Graphene Composite as Chemical Anchor of Polysulfides for Lithium-Sulfur Batteries. *Nat. Commun.* **2017**, *8* (1), 14627. https://doi.org/10.1038/ncomms14627.

(34) Wu, M.; Guo, H.; Lin, Y. N.; Wu, K.; Ma, T.; Hagfeldt, A. Synthesis of Highly Effective Vanadium Nitride (VN) Peas as a Counter Electrode Catalyst in Dye-Sensitized Solar Cells. *J. Phys. Chem. C* **2014**, *118* (24), 12625–12631. https://doi.org/10.1021/jp501797e.

(35) Wicher, B.; Chodun, R.; Nowakowska-Langier, K.; Trzcinski, M.; Skowroński, L.; Okrasa, S.; Minikayev, R.; Naparty, M. K.; Zdunek, K. Chemical and Structural Characterization of Tungsten Nitride (WNx) Thin Films Synthesized via Gas Injection Magnetron Sputtering Technique. *Vacuum* **2019**, *165* (February), 266–273. https://doi.org/10.1016/j.vacuum.2019.04.020.

(36) Simon, P.; Gogotsi, Y. Materials for Electrochemical Capacitors. *Mater. Sustain.*

Energy A Collect. Peer-Reviewed Res. Rev. Artic. from Nat. Publ. Gr. **2010**, 138–147. https://doi.org/10.1142/9789814317665_0021.

TOC graphic

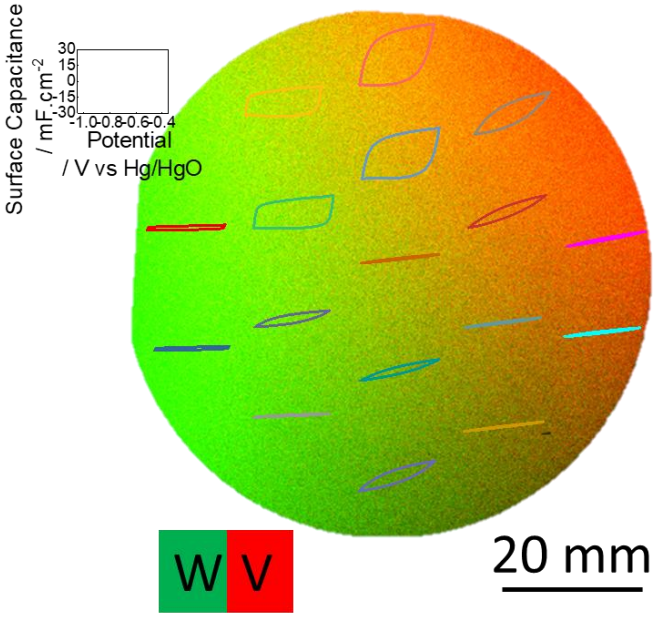

Wafer-scale evolution of electrochemical surface capacitance superimposed with chemical mapping